Applied Catalysis B: Environmental 309 (2022) 121279

Contents lists available at ScienceDirect

Applied Catalysis B: Environmental

journal homepage: www.elsevier.com/locate/apcatb

Interface engineering of *in−situ* formed nickel hydr(oxy)oxides on nickel nitrides to boost alkaline hydrogen electrocatalysis

Jin-Tao Ren [a], Yan-Su Wang [a], Yue-Jun Song [b], Lei Chen [a], Zhong-Yong Yuan [a,*]

[a] Key Laboratory of Advanced Energy Materials Chemistry (Ministry of Education), School of Materials Science and Engineering, Nankai University, Tianjin 300350, China

[b] School of Investigation, China People's Police University, Langfang 065000, China

ARTICLE INFO

Keywords:
Nickel nitrides
Nickel hydr(oxy)oxides
Heterostructure engineering
Hydrogen oxidation
Hydrogen evolution

ABSTRACT

Highly efficient platinum−group−metal (PGM) free catalysts for alkaline hydrogen oxidation reaction (HOR) are of vital issues for the development of alkaline hydroxide exchange membrane fuel cells (HEMFCs). Herein, with the help of interface engineering by the *in−situ* electrochemical surface reconfiguration strategy, the seamless nickel nitrides-nickel hydr(oxy)oxide (denoted as Ni_3N−$Ni(OH)_2$) heterostructures were developed. From the systematic electrochemical measurements, the impressive HOR performance such as nearly zero onset overpotential, larger exchange current density, excellent long−term durability, and robust CO tolerance in alkaline media, are obtained by the optimized Ni_3N−$Ni(OH)_2$ catalyst, thus rendering it significant potential for applications in HEMFCs. Furthermore, this catalyst also exhibits superior HER activity, approaching to that of Pt/C catalyst. The tailored *d* band center of Ni and the enhanced hydroxyl adsorption ability at Ni_3N−$Ni(OH)_2$ heterojunctions are evidenced by the comprehensive spectroscopy and electrochemical analyses, which are favorable for the accelerated Volmer step toward alkaline hydrogen electrocatalysis.

1. Introduction

Hydrogen (H_2) is considered as the clean and carbon−neutral fuel carrier in the field of sustainable energy, for instance, the utilization of H_2 through hydrogen fuel cell will only supply electricity with water as the sole product [1,2]. The conversion efficiency of H_2 strongly depends on the efficient hydrogen oxidation reaction (HOR), in that the multi−protons and electrons properties of HOR always need electrocatalysts to achieve industrially relevant rates. To date, platinum group metal (PGM) catalysts exhibit extraordinary HOR performance in acidic electrolyte, whereas the unfavorable cost of Pt and the demanding conditions of acidic electrolyte for earth−abundant materials have attracting huge attention to engineer transition metal electrocatalysts for HOR in alkaline electrolyte [3,4]. However, the decreased HOR performance in alkaline media, even for Pt catalysts, is nearly two orders of magnitude lower than that in acidic electrolyte [5,6]. Hence, it is of vital to design highly competent and affordable PGM−free HOR catalysts for promising hydrogen electrochemistry.

At present, relatively less attention was devoted to the engineering of nonprecious HOR catalysts. Usually, the critical intermediates, adsorbed hydrogen (H_{ads}) on the surface of electrocatalysts, have been widely accepted as the important descriptor in evaluating the activity of the desirable materials for HOR [7,8]. Hence, a large amount of efforts have been focused on optimizing Gibbs free energy of hydrogen adsorption (ΔG_{H^*}) of diverse electrocatalysts [9,10]. Although the great efforts in advancing HOR activities of earth abundant electrocatalysts, to date, only nickel−based electrocatalysts exhibit promising HOR potential to meet industrial applications [11,12]. Nevertheless, the relatively higher ΔG_{H^*} on pure Ni metal (about −0.30 eV) [6] always requires some suitable strategies to tailor the electronic structure of Ni sites, such as, alloying, defect introduction, surface modification, molecular design, and composition tuning, thereby tuning their interaction with reaction intermediates [13,14]. For instance, the strained Ni nanoparticles derived from Ni-based MOFs reported by Hu's group exhibits the state-of-the-art mass-specific kinetic current activity of 50 A g^{-1} for alkaline HOR under the optimal conditions [15]. Li et al. demonstrated that allowing Ni with Mo obtained the record-high mass activity of 79 A g^{-1} [16]. On the other hand, the alkaline HOR mechanism is normally accepted to proceed through the bi-functional theory (although different views exist), namely, the adsorption of hydrogen (H_{ads}) and hydroxyl (OH_{ads}) intermediates on the electrocatalysts surface are both critical for Volmer step ($M{-}H_{ads} + OH^- \rightarrow H_2O + e^- + M$, M represents the surface

* Corresponding author.
E-mail address: zyyuan@nankai.edu.cn (Z.-Y. Yuan).

https://doi.org/10.1016/j.apcatb.2022.121279
Received 18 November 2021; Received in revised form 17 February 2022; Accepted 2 March 2022
Available online 3 March 2022

active sties) during alkaline HOR process [17,18]. For example, the Ni/NiO/C catalysts with the controllable Ni-NiO heterojunctions were synthesized by Sun's group [19], which exhibited the improved alkaline HOR performance compared to their single Ni− or NiO−based counterparts, wherein the metal Ni promotes the adsorption of hydrogen and the NiO acts as the hydroxyl adsorption sites. Lou et al. boosted the HOR performance of Ni in alkaline electrolyte by coupling with oxygen-vacancy-rich CeO_2 nanoparticles [20]. These studies demonstrate the possibility for developing low-cost and efficient Ni-based materials toward HOR in alkaline electrolyte on the basis of bi-functional theory. Although the numerous efforts in improving the alkaline HOR activity of low-cost catalysts, it is still a huge HOR activity gap between PGM electrocatalysts and PGM−free Ni−based materials.

Transition metal nitrides, such as Ni_3N, represent as one of novel category of catalysts with huge potential for electrocatalytic reactions. Benefiting from the accumulated positive charge on Ni sites by N element alloying, the ΔG_{H^*} on the favorable planes of Ni_3N significantly decreased to − 0.05 eV, very close to that of Pt sites [21]. Meanwhile, this has been considered that the metal hydr(oxy)oxides, especially, Ni$(OH)_2$, would accelerate water dissociation and stabilize hydroxyl groups in alkaline electrolyte [22]. Therefore, the simultaneous coupling Ni_3N with $Ni(OH)_2$ is highly expected to fully inspire the merits of each active species and thereby to systematically accelerate the reaction kinetics toward HOR based on the consideration of bi-functional theory. With respect to interface coupling effect, the intimate integration of different active components into the current support with hierarchically porous structure and high conductivity is also significant for boosting performance, which would supply large electrochemical surface sites and fast charge transfer owing to the reduced Schottky barrier at electrode-catalyst interface [23]. However, it should be noted that the seamless heterointerface engineering of each component toward HOR catalysts has been scarcely considered. Also, no relevant interest has focused on the systematic and understanding of surface engineering of Ni_3N in the improved HOR activity.

Herein, from the consideration of interface modification by different components, the rich nickel nitride-nickel hydr(oxy)oxide (named as Ni_3N−$Ni(OH)_2$) heterojunctions were well-designed through the electrodeposition of Ni nanoparticles on nickel foam (NF) followed by thermal nitridation in ammonia, subsequently following *in−situ* electrochemical surface reconfiguration (ESR) under the controllable anodic treatment. By virtue of the interface engineering with seamless heterojunctions, the strong electronic coupling in Ni_3N−$Ni(OH)_2$ renders Ni_3N negatively charged. As expected, the resultant Ni_3N−Ni$(OH)_2$/NF demonstrates excellent HOR activity, which nearly rivals that of Pt/NF benchmark in alkaline electrolyte. Even more impressive is that this Ni_3N−$Ni(OH)_2$/NF still exhibits nearly Pt−like performance for hydrogen evolution reaction (HER) in alkaline electrolyte. This work thoroughly investigate the interface interaction between Ni_3N and nickel hydr(oxy)oxides, which would provide some novel inspiration and guidance for the design and fabrication of high-efficiency metal nitrides for electrocatalysis.

2. Experimental section

2.1. Fabrication of Ni_3N/NF

Typically, the cathodic electrodeposition of nickel microspheres onto nickel foam was performed in the electrolyte consisting of 2.0 M NH_4Cl and 0.1 M $NiCl_2.6H_2O$ with the two electrode configuration at the current density of − 1.0 A cm^{-2} for 600 s. Following, the obtained materials was subjected to nitridation under flowing NH_3 at 350 ℃ for 3 h to obtain fresh Ni_3N/NF catalysts.

2.2. Fabrication of Ni_3N−$Ni(OH)_2$/NF

Subsequently, the fresh Ni_3N/NF was suffered from the cyclic voltammetry for five cycles between 1.20 and 1.60 V vs. RHE with the scan rate of 30 mV s^{-1} in 1.0 M KOH. The resultant product was Ni_3N−$Ni(OH)_2$/NF.

2.3. Fabrication of Ni_3N+$Ni(OH)_2$/NF

The common post arranging method was developed to fabricate the Ni_3N+$Ni(OH)_2$/NF catalysts through electrodepositing nickel hydroxide onto the surface of fresh Ni_3N/NF in 6 mM $Ni(NO_3)_2.6H_2O$ aqueous solution with three−electrode configuration at the constant potential of − 1.0 V vs. Ag/AgCl for 300 s. The finally obtained sample was Ni_3N+Ni$(OH)_2$/NF.

2.4. Electrochemical measurements

The electrochemical measurements were conducted by using a computer−controlled CHI 760E electrochemical workstation with a three−electrode cell system. The resultant electrocatalysts was directly used as the working electrode. A calibrated Ag/AgCl (saturated KCl) and the carbon rod were used as the reference and counter electrode, respectively. The electrolyte for HER was 1.0 M KOH (pH 13.60) and for HOR was 0.1 M KOH (pH 12.80). All electrolytes were bubbled with H_2 throughout the whole electrochemical experiments. All potentials are reported versus reversible hydrogen electrode (RHE). Unless stated otherwise, all LSV polarization curves for HOR were not *iR*−corrected and obtained by scanning from negative to positive potential. For HOR tests, the slow scan rate of 1 mV s^{-1} was conducted to obtain the LSV curves to minimize the capacitive current background. All electrolytes were bubbled with H_2 throughout the whole electrochemical experiments. The catalytic stability for HER/HOR was evaluated by either chronopotentiometry (CP) or chronoamperometry (CA) measurement. Commercial Pt/C catalysts loaded on nickel foams were also used as working electrodes for both HER and HOR. The current densities in this work were calculated on the basis of the geometric areas, or electrochemically active surface areas (ECSAs) of electrodes.

Other details of Characterization and Electrochemical measurements were provided in Supporting Information (SI).

3. Results and discussion

3.1. Materials synthesis and characterization

The Ni_3N − $Ni(OH)_2$/NF was fabricated by the continuous three steps, namely, cathodic electrodeposition, low−temperature nitridation, and *in−situ* electrochemical surface reconfiguration (ESR) route. The total synthesis procedures were schematically illustrated in Fig. 1a. Different to the smooth surface of pristine nickel foam (Fig. S1), from the corresponding SEM images (Fig. S2), the cathodic electrodeposition achieves lots of stacked coarse nanoparticles over the skeleton surface, which facilitates the infiltration of electrolyte and enhance the effective contact area of electrolyte and electrode. Suffering from the low temperature nitridation under flowing ammonia, the microspheres formed macroporous ligament network are still maintained (Fig. S3a-c). The high-resolution TEM (HR-TEM) images disclose the detailed nanostructure of the formed materials. In Fig. S3d, the well-crystallized lattice fringes with the interplanar spacing of 0.231 nm are assigned to the (110) crystal plane of hexagonal Ni_3N.

Then, to get the *in−situ* formed surface hydr(oxy)oxides layer, the mild electrochemical surface reconfiguration with CV cycles was conducted in alkaline electrolyte. Fig. S4 displays the CV curves of Ni_3N/NF under different cycles, wherein the evident peaks occurring at the potential at about 1.40 V vs. RHE are caused by the surface oxidation of Ni^{2+} to Ni^{3+}. With the continuous operation, the oxidation peaks gradually shift to higher potential and the peak areas also increase, revealing the formation of more surface hydr(oxy)oxide components. The SEM image in Fig. 1b exhibits the stacked nanoparticles are well

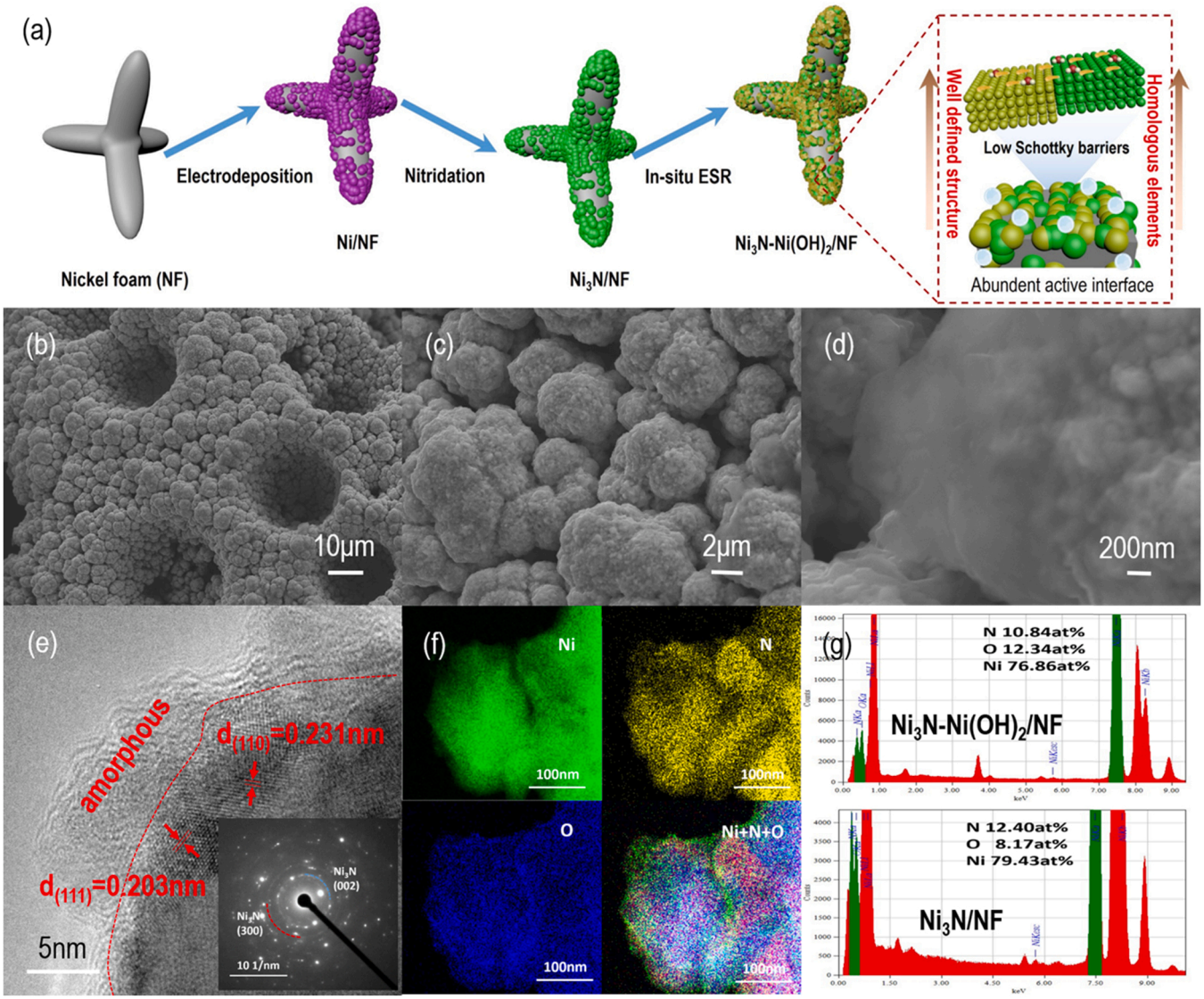

Fig. 1. (a) Schematic illustration of the preparation procedures for Ni_3N−$Ni(OH)_2$/NF. (b) SEM image of Ni_3N/NF. (c,d) SEM and (e) TEM images of Ni_3N−$Ni(OH)_2$/NF. (f) TEM elemental mapping images of Ni_3N−$Ni(OH)_2$/NF. (g) EDX result of Ni_3N−$Ni(OH)_2$/NF and Ni_3N/NF.

retained after the ESR treatments. And the further magnification in Fig. 1c and d present the flocculent nanosheets that is partially adhered to the surface of the underlying stacked microparticles, which is significantly different from the loose covering of $Ni(OH)_2$ nanosheet on microparticles for Ni_3N + $Ni(OH)_2$/NF (Fig. S5) that is synthesized by post−electrodeposition of $Ni(OH)_2$ nanosheets on fresh Ni_3N/NF. The characteristic uniform dispersion of surface hydr(oxy)oxides species is beneficial to interface electron transfer and interaction during electrocatalysis [24]. In the high-resolution TEM image (Fig. 1e) for Ni_3N−$Ni(OH)_2$/NF, the amorphous ultrathin shell with the thickness of about 5 nm is uniformly covering on the surface of the nanoparticles with well crystallinity, revealing the successful preparation of interfaces, which is conductive to the charge transfer [23]. These poorly crystalline shell layers should be ascribed to the amorphous hydr(oxy)oxides materials during the anodic reconstruction process [25]. And the well−resolved lattice fringes with inter−planar spacing of 0.231 and 0.203 nm of the inside core are ascribed to the (110) and (111) planes of hexagonal Ni_3N, respectively. The elemental mapping images (Fig. 1f) of Ni_3N−$Ni(OH)_2$/NF exhibit the uniformly distribution of Ni, N, and O elements. Moreover, the overlay elemental mapping result of Ni_3N−$Ni(OH)_2$/NF confirms the homogeneous distribution of O elements throughout entire microspheres, declaring the uniform surface oxidation of Ni_3N. And the energy dispersive X−ray (EDX) spectrum verifies the relatively lower O content of 8.17 at% for Ni_3N/NF (Fig. 1g) compared to that of the surface oxidized Ni_3N−$Ni(OH)_2$/NF (12.34 at%), further manifesting the formation of outer hydr(oxy)oxides layer.

The XRD patterns in Fig. 2a corroborate the new peaks centered at $2\theta = 38.94°$ and $42.11°$ with depressed intensity after nitridation, corresponding to the (110) and (002) facets of hexagonal Ni_3N phase (JCPDS # 10−0280), whereas the major diffraction peaks located at $2\theta = 44.51°$, $51.85°$, and $76.37°$ ascribed to cubic Ni phase (JCPDS # 04 −0850) are still remained, which should be assigned to the current collector of nickel foam. And the identical diffraction peaks for Ni_3N−$Ni(OH)_2$/NF relative to Ni_3N/NF are still observed after mild surface reconfiguration, which is largely due to the ultrathin thickness of hydr(oxy)oxides layer on Ni_3N microspheres. It is observed that no diffraction peaks ascribed to the nickel hydr(oxy)oxides species are observed on those XRD pattern, which should be attributed to the existence of outer amorphous species on crystal Ni_3N core. The diffraction peak intensity of Ni_3N−$Ni(OH)_2$/NF is slightly lower compared to Ni_3N/NF because the introduction of surface hydr(oxy)oxides layer disrupts the long-range order of Ni_3N, and thereby obtaining the decreased crystallinity. Raman spectra in Fig. S7 evidently exhibits the broad and high peak about 520 cm^{-1}, which is ascribed to the stretching vibration of

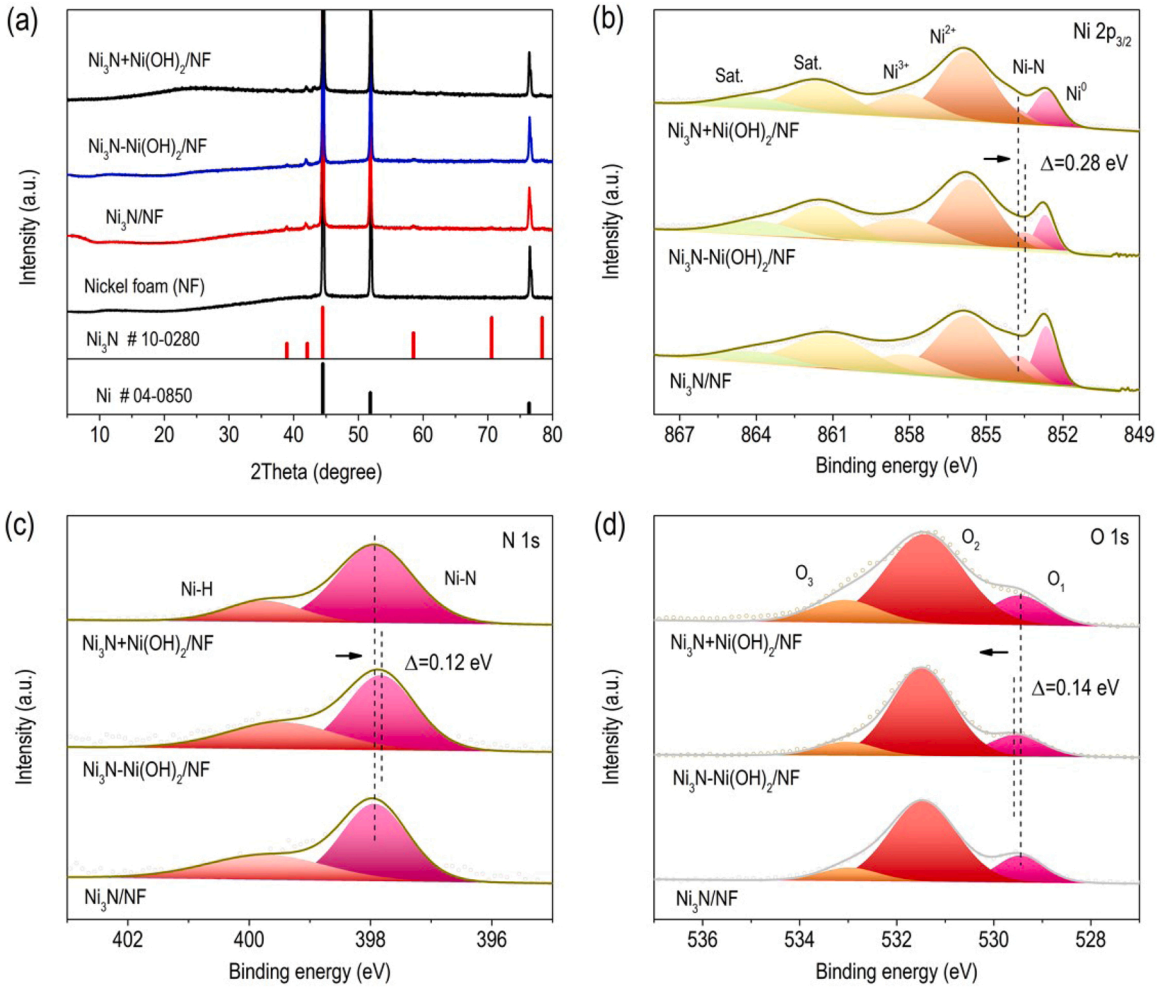

Fig. 2. (a) XRD patterns of $Ni_3N{-}Ni(OH)_2$/NF, $Ni_3N{+}Ni(OH)_2$/NF, Ni_3N/NF, and Ni/NF. High−resolution XPS Ni $2p_{3/2}$ (b), N 1s (c), and O 1s (d) spectra of $Ni_3N{-}Ni(OH)_2$/NF, $Ni_3N{+}Ni(OH)_2$/NF, and Ni_3N/NF.

hydr(oxy)oxides [26].

The intimate interaction of surface $Ni_3N{-}Ni(OH)_2$ heterostructures for $Ni_3N{-}Ni(OH)_2$/NF would lead to significant electronic coupling and the changed surface charge states of Ni_3N, which are confirmed by XPS characterization between $Ni_3N{-}Ni(OH)_2$/NF and Ni_3N/NF. Determining from their XPS survey scan in Fig. S8, the evident O signal of $Ni_3N{-}Ni(OH)_2$/NF exhibits a higher surface oxygen content of 72.61 at %, 1.12 times to that of Ni_3N/NF, which is consistent with their EDX result, further indicating the formation of surface hydr(oxy)oxides layer. With respect to high−resolution Ni $3p_{3/2}$ spectra (Fig. 2b), the fitted features with the binding energies of 852.69, 853.55, 855.68, and 858.27 eV are assignable to Ni^0 of nickel foam substrate, Ni−N of Ni_3N, as well as Ni^{2+} and Ni^{3+} species of surface nickel hydr(oxy)oxides species, respectively [27,28]. The satellite (Sat.) peak at 861.47 and 864.11 eV attributes to the shake−up excitation of the high−spin nickel species [29]. The high−resolution N 1s spectrum (Fig. 2c) for $Ni_3N{-}Ni(OH)_2$/NF is deconvoluted into two subpeaks located at 397.93 and 399.76 eV, which are related to N components of Ni_3N and N−H moieties resulted from the incomplete nitridation with NH_3, respectively [30–32]. Such similar peak deconvolution related to Ni 2p and N 1 s are still observed for Ni_3N/NF and $Ni_3N{+}Ni(OH)_2$/NF. And the O 1s signal (Fig. 2d) is fitted into three peaks, including oxygen coordinated metal (O_1), bound hydroxides groups (O_2), as well as the physically adsorbed oxygen or water (O_3) [33]. Moreover, from the XPS spectra related to Ni_3N/NF and $Ni_3N{-}Ni(OH)_2$/NF, the decreased relative intensity between low energy and high energy peaks for each targeted elements further demonstrates the more hydr(oxy)oxides formed during surface ESR process. The nearly identical binding energies of Ni−N for Ni_3N/NF and $Ni_3N{+}Ni(OH)_2$/NF indicate negligible interface electron transfer and coupling interaction between inner Ni_3N and covered hydr(oxy) oxides layer in $Ni_3N{+}Ni(OH)_2$/NF. In contrast, the binding energy of Ni−N for $Ni_3N{-}Ni(OH)_2$/NF negatively shifts about 0.12 eV compared to Ni_3N/NF, suggesting significant electron transfer from hydr(oxy)oxides species to Ni_3N resulted from the strong electron coupling effect. And the high−resolution N 1s and O 1s XPS spectra also exhibit the shifted binding energies, further verifying the close assembly and strong electronic interaction between nickel nitrides and *in-situ* formed nickel hydr(oxy)oxides due to the construction of coupling interface in $Ni_3N{-}Ni(OH)_2$/NF. In other words, the Ni atoms in Ni_3N receive electrons transferred from surface hydr(oxy)oxides layer, and the interfacial interaction increase the number of unoccupied electron on O atoms, wherein the negative charging of Ni sites in Ni_3N would optimize of the surface adsorption of H* and water toward HER, while the surface hydr (oxy)oxide layer is favorable for the adsorption of OH* species during HOR process, together endowing the significant bifunctionality for HOR and HER in alkaline media [34,35]. Besides the interface electronic regulation, the surface wettability of electrodes still hold the important influence on the electrochemical adsorption behavior of reactants. Water contact angle measurements in Fig. S9 exhibits the nearly 0° for contact angle of $Ni_3N{-}Ni(OH)_2$/NF, exhibiting the superhydrophilic property for the favorable contact between electrolyte and electrode surface.

3.2. Electrocatalytic alkaline hydrogen oxidation

Electrocatalytic HOR performance of the as−fabricated materials was first tested through steady−state LSV in 0.1 M KOH with H_2 saturation. Benefiting from their integrated electrode configuration, those electrodes with controllable size were directly employed as working electrode for electrocatalytic measurements, and the corresponding current density of each catalysts was determined by normalizing their geometric area of electrodes. To minimize the capacitive current background (Fig. S10), all the HOR polarization curves of those fabricated materials were recorded at the current density of 1 mV s^{-1}. Prior to electrochemical measurements, the effect of electrodeposition time, nitridation temperature, and anodic oxidation duration of Ni_3N−Ni $(OH)_2$/NF on the electrochemical activities were investigated. As displayed in Fig. S11 and Fig. S12, the sample of Ni_3N−$Ni(OH)_2$/NF synthesized with electrodeposition time of 600 s, nitridation temperature of 350 ℃, and oxidation duration of 5 cycles exhibits the best hydrogen electrochemistry activities. Thus, all the following measured samples were prepared at such optimal fabrication conditions unless noted otherwise. And the commercial Pt/C (20 *wt*%) coated nickel foam was fabricated as the control sample of Pt/NF for the purpose of comparison. Before electrocatalytic activities measurement, the reference electrode calibration was conducted (Fig. S13).

Different to the slight capacitance current achieved in Ar saturation (Fig. S14), Ni_3N−$Ni(OH)_2$/NF exhibits the evident current density between 0 and 0.20 V vs. RHE in H_2 −saturated electrolyte, verifying the occurrence of H_2 oxidation. From their LSV curves in Fig. 3a, without nitridation, the pristine Ni/NF shows rather poor HOR behavior, which should be attributed to the high adsorption capacity of reaction intermediate H*. Upon treated in flowing NH_3, the formed Ni_3N/NF exhibits increased current, which presents the positive effect aroused from interaction between Ni and N atoms. And the higher activity of Ni_3N/NF relative to that of nitrided nickel foam (N−NF) highlights the positive effect of utilizing stacked coarse nickel nanospheres over the skeleton surface for the preparation of nickel nitrides. In particular, after coupling with surface $Ni(OH)_2$ layer through the post−electrodeposition approach, the anodic current of Ni_3N+$Ni(OH)_2$/NF is further boosted, highlighting the positive impact of the anchoring of $Ni(OH)_2$, which implies that the coupling of $Ni(OH)_2$ generates positive effect on the electrocatalytic activities of Ni_3N toward HOR. However, the *in-situ* formation of hydr(oxy)oxides layer on Ni_3N−$Ni(OH)_2$/NF induces largely enhanced current density, which should be the more significant coupling interaction between Ni_3N and *in−situ* formed hydr(oxy)oxides layer. Noticeably, for those Ni−based electrocatalysts, their HOR current densities come to decline when anodically scanning over approximately 0.15 V vs. RHE, which is ascribed to the surface oxidation of Ni_3N at higher potential. In fact, at the applied potential of 0.05 V vs. RHE, the current density of Ni_3N−$Ni(OH)_2$/NF is 1.51 mA cm^{-2}, which is larger than those of Ni_3N+$Ni(OH)_2$/NF (1.03 mA cm^{-2}), Ni_3N/NF (0.71 mA cm^{-2}), N−NF(0.69 mA cm^{-2}), and Ni/NF (0.12 mA cm^{-2}), even approaches to Pt/NF (1.76 mA cm^{-2}).

It is widely accepted that the positively charged transition metal oxides and hydroxides are valid catalysts for the accelerated water dissociation and favors more adsorption of electron−rich OH^- in H_2O. Inspired by this consideration, several Ni−based materials−transition metal oxides formed hybrid catalysts such as Ni/MoO_2 [5], Ni/CeO_2 [20], NiMo [36], have been developed for alkaline HOR. For those hybrids, the metal Ni−based materials facilitate the H_{ads} adsorption and the metal oxides promote the adsorption of OH_{ads} [24]. Furthermore, the interface interaction for those hybrid catalysts would alter the electron configuration of Ni−based materials, which thereby further optimize the ΔG_{H^*} on Ni sites, thus resulting in the improved HOR performance.

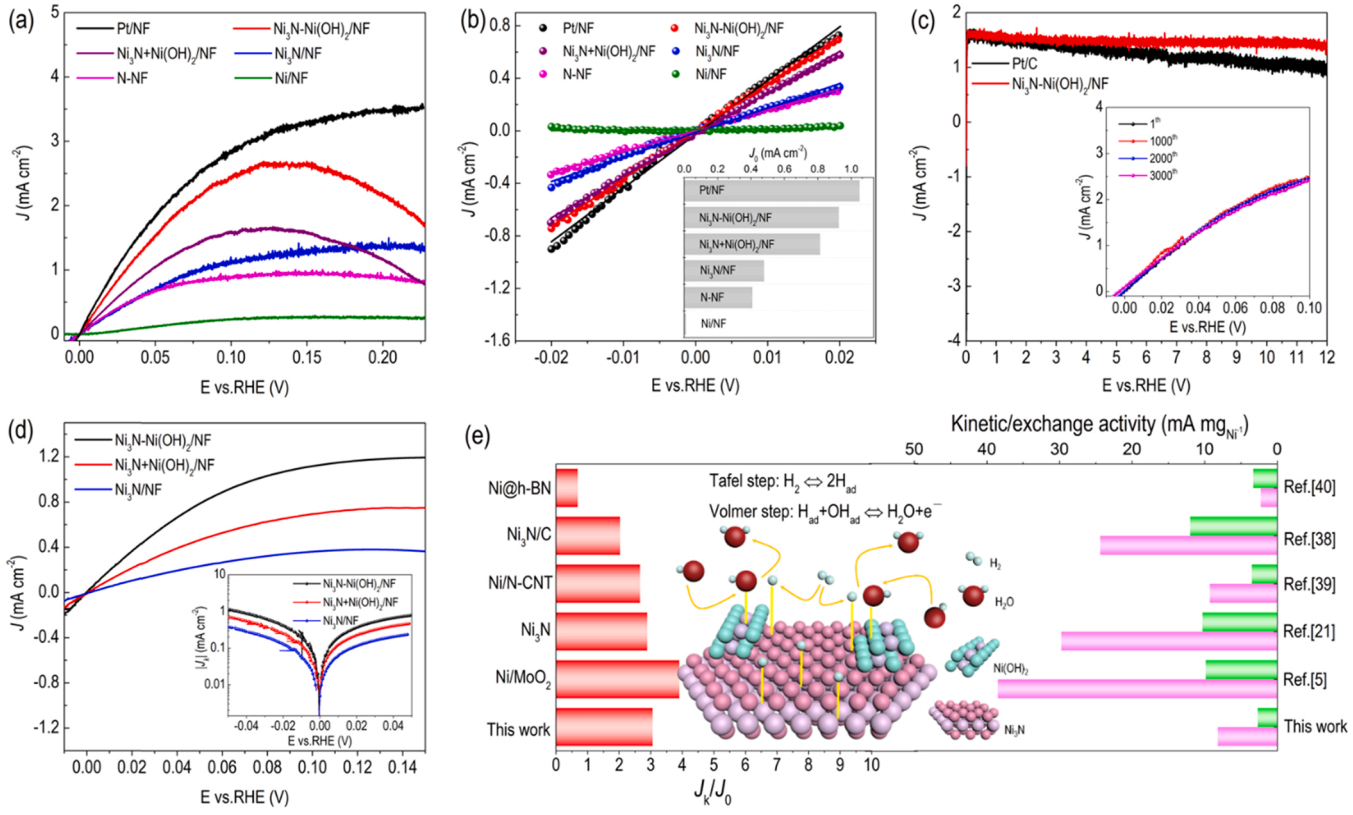

Fig. 3. a. (a) HOR polarization curves and (b) micro−polarization region of the prepared catalysts in H_2 −saturated 0.1 M KOH. (c) Chronoamperometry measurements of Ni_3N−$Ni(OH)_2$/NF and Pt/NF at overpotential of 50 mV. Inset is the HOR polarization curves of Ni_3N−$Ni(OH)_2$/NF during continuous CV tests. (d) HOR polarization curves of different powder catalysts on RDE in H_2−saturated 0.1 M KOH. Inset is the Tafel plots derived from their LSV curves. (e) Comparison of J_{mk}/J_{m0}, mass kinetic and exchange activity of Ni_3N−$Ni(OH)_2$ with previous studies mentioned in the literature.

On the basis of such HOR activity tendency of those electrocatalysts including Ni_3N/NF, Ni_3N+$Ni(OH)_2$/NF, and Ni_3N−$Ni(OH)_2$/NF as well as the reported studies [21], it is preliminarily indicates that the Ni_3N−$Ni(OH)_2$ interfacial sites with low−valence Ni-N species are the main active contributor of HOR and their HOR activity is dependent of their chemical valence of Ni sites.

The exchange current density (J_0) of those fabricated catalysts were investigated from the micro−polarization region within the narrow potential range from − 20–20 mV vs. RHE (Fig. 3b). The determined J_0 of Ni_3N−$Ni(OH)_2$/NF is 0.93 mA cm^{-2}, which is close to that of Pt/NF (1.05 mA cm^{-2}), but nearly 1.14, 1.94, and 2.27 times than that of Ni_3N + $Ni(OH)_2$/NF, Ni_3N/NF, and N−NF, respectively. Such observation indicates the enhanced specific activity of Ni_3N−$Ni(OH)_2$/NF toward alkaline HOR. Furthermore, in order to access the intrinsic specific activity of each electrocatalysts, their eletrocatalytic activities were normalized by their electrochemical surface area (ECSA) (Fig. S15). Apparently, in Fig. S16, Ni_3N−$Ni(OH)_2$/NF shows largest specific activity, higher than that of Ni_3N+$Ni(OH)_2$/NF and Ni_3N/NF. The intrinsic HOR activity of the catalysts was further evaluated by evaluating their turnover frequency (TOF) per total surface sites. Herein, all surface Ni sites are presumed to take part in HOR, and thereby the lower value of TOF is achieved. At the potential of 0.10 V vs. RHE (Fig. S17), the determined TOF of Ni_3N−$Ni(OH)_2$/NF is 0.066 s^{-1}, being 1.41, and 1.58 times than Ni_3N+$Ni(OH)_2$/NF and Ni_3N/NF, respectively. This evidently indicates that the great HOR activity of Ni_3N−$Ni(OH)_2$/NF origins not only from larger ECSA thus sufficient active sites but also from improved intrinsic activity.

Moreover, Ni_3N-$Ni(OH)_2$/NF exhibits robust stability on the basis of the accelerated degradation measurement, wherein the 3000th LSV nearly overlaps the initial curve in the inset of Fig. 3c and its chronoamperometry electrolysis with almost stable current output is preserved over 12 h within H_2−saturated electrolyte in Fig. 3c, as well as according to its structure and morphology experiment on XRD pattern and SEM images (Fig. S18) after the stability examination. In addition, the sustaining current of Ni_3N−$Ni(OH)_2$/NF during the long−term testing period further demonstrate that the anodic current is surely inducted by the hydrogen oxidation process. On the contrary, the $i-t$ curve of Pt/NF (Fig. 3c) exhibits the evident current drop with the extension of testing time. Since the poor adhesion of Nafion binder for Pt/NF, the gradual abscission of Pt/C from nickel foam results in the fading of HOR activity, while the robust interaction between nickel foam substrate and Ni_3N superstructure ensures the excellent stability of Ni_3N−$Ni(OH)_2$/NF.

The superior tolerance to CO impurity is also another necessary requirement of HOR catalysts in HEMFCs because the steam reforming from hydrocarbons produced H_2 that is the current industrial production approach, always contains CO impurity. As shown on their LSV curves in Fig. S19, the anodic HOR current of Pt/NF indeed is evidently suppressed when the CO−containing H_2 is pumped into the KOH electrolyte relative to that in pure H_2 condition, for example, the anodic current of Pt/NF decreases from 2.85 to 1.17 mA cm^{-2} at 0.10 V vs. RHE. It should be noted that the polarization curve of Pt/NF does not pass through zero point, which should be ascribed to that the CO adsorption on the surface of Pt sites reduces the surface hydrogen coverage, resulting in the skewing of hydrogen evolution−hydrogen oxidation equilibrium potential [5,37]. In contrast, Ni_3N−$Ni(OH)_2$/NF only exhibits slight current fluctuation under the identical condition. This stability performance unambiguously manifests this developed Ni_3N−$Ni(OH)_2$/NF showing excellent long−term stability and CO tolerance for alkaline HOR, associated with the nearly Pt−like HOR activities, which renders it an attractive electrocatalyst for sustainable H_2 oxidation.

Next, the electrocatalytic performance of Ni_3N−$Ni(OH)_2$ powder obtained from Ni_3N−$Ni(OH)_2$/NF by the ultrasound was further measured to reflect its intrinsic HOR behavior. In addition, the other reference catalyst powders were also obtained with the similar method to that for Ni_3N−$Ni(OH)_2$. The metal−based catalyst powder with Nafion binder was uniformly coated onto the glassy carbon rotating disk electrode (RDE) with the active materials loading of 0.20 mg cm^{-2}. When the electrode rotation speed ranges from 400 to 2500 rpm, as reflected on their LSV curves in Fig. S20a, all the anodic polarization curves exhibit the sharply increased current density until the overpotential raise to about 0.10 V vs. RHE, which should be ascribed to the diffusion−controlled reaction kinetic process. And the evident anodic Ni oxidation behavior at around 0.20 V vs. RHE is also observed for those Ni−based catalysts on their polarization curves measured from RDE instrument (Fig. S20b). Moreover, the HOR activities of all those powder catalysts follow the same activity tendency to their self−supported configuration in Fig. 4d. For instance, at 0.05 V vs. RHE, the current density of Ni_3N − $Ni(OH)_2$ reaches about 0.81 mA cm^{-2} at the rotation speed of 1600 rpm, which is evidently larger than that of Ni_3N + $Ni(OH)_2$ (0.47 mA cm^{-2}) and Ni_3N (0.24 mA cm^{-2}). The representative HER-HOR Tafel plots of kinetic current densities for Ni_3N−$Ni(OH)_2$, Ni_3N+$Ni(OH)_2$, and Ni_3N were plotted in the inset of Fig. 4d. All the samples show the symmetrical kinetic current density-potential curves, revealing the Volmer-dominated Tafel-Volmer reaction process toward HOR.

The LSV curves at different rotation speeds are further measured to investigate the mass−specific activity of electrocatalysts. As depicted in Fig. S20a, the raised rotation rate with faster mass transfer leads to the increased anodic current. By fitting the J^{-1} with $\omega^{-1/2}$ according to the dictation of the Koutecky–Levich equation in the inset of Fig. S20a, the slope is 8.09 cm^2 mA^{-1} $s^{-1/2}$ at 0.05 V vs. RHE. For a further step, the kinetic current density (J_k) of 1.52 mA cm^{-2} and the mass−specific kinetic current (J_{mk}) of 8.21 mA mg_{Ni}^{-1} are obtained. Furthermore, the exchange current density (J_0) of Ni_3N−$Ni(OH)_2$ is 0.51 mA cm^{-2} by fitting the Butler–Volmer equation in the micro−polarization range (Fig. S21). The determined J_0 of Ni_3N − $Ni(OH)_2$ is still higher than other nickel−based catalysts. And the mass−specific exchange current (J_{m0}) is determined to be 2.68 mA mg^{-1}. Since the values of J_{mk} and J_{m0} are significantly dependent on the electrocatalyst loading on RDE on the basis of previous works [5], therefore, a descriptor of J_{mk}/J_{m0} is defined to reflect the mass kinetics performance of HOR electrocatalysts. The activity of previous mentioned Ni−based HOR catalysts are shown in Fig. 3e, and their J_{mk}/J_{m0} values are also plotted. The J_{mk}/J_{m0} of Ni_3N−$Ni(OH)_2$ is better than that of some catalysts such as Ni/MoO_2 [5], Ni_3N [21], Ni_3N/C [38], Ni/N−CNT [39], and Ni@h−BN [40], verifying the higher electrocatalytic activity. Thus, the high HOR performance of Ni_3N−$Ni(OH)_2$ measured on RDE compared with other previous Ni−based electrocatalysts further demonstrate the great intrinsic hydrogen oxidation activities of Ni_3N−$Ni(OH)_2$ in alkaline electrolyte.

To get further insight into the HOR mechanism occurred on Ni_3N−$Ni(OH)_2$/NF, its HER activity in alkaline solution was examined. Typically, alkaline HER of non−noble metal electrocatalysts involves first water adsorption and dissociation to form the adsorbed H intermediate (Volmer reaction) followed by H_2 formation (Heyrovsky step or Tafel step), as shown on the following pathways:

$$H_3O^+ + e^- \rightarrow H_{ads} + H_2O \text{ (Volmer step)}$$

and.

$$H_{ads} + H_3O^+ + e^- \rightarrow H_2 + H_2O \text{ (Heyrovsky step)}$$

or.

$$H_3O^+ + e^- \rightarrow H_{ads} + H_2O \text{ (Volmer step)}$$

and.

$$H_{ads} + H_{ads} \rightarrow H_2 \text{ (Tafel step)}$$

and thereby the ability of adsorption of H_{ads} intermediate species on the electrocatalyst surface is important to HER. As generally accepted, the HOR mechanism in alkaline condition is normally accepted to proceed by either the Tafel−Volmer step or the Heyrovsky−Volmer step:

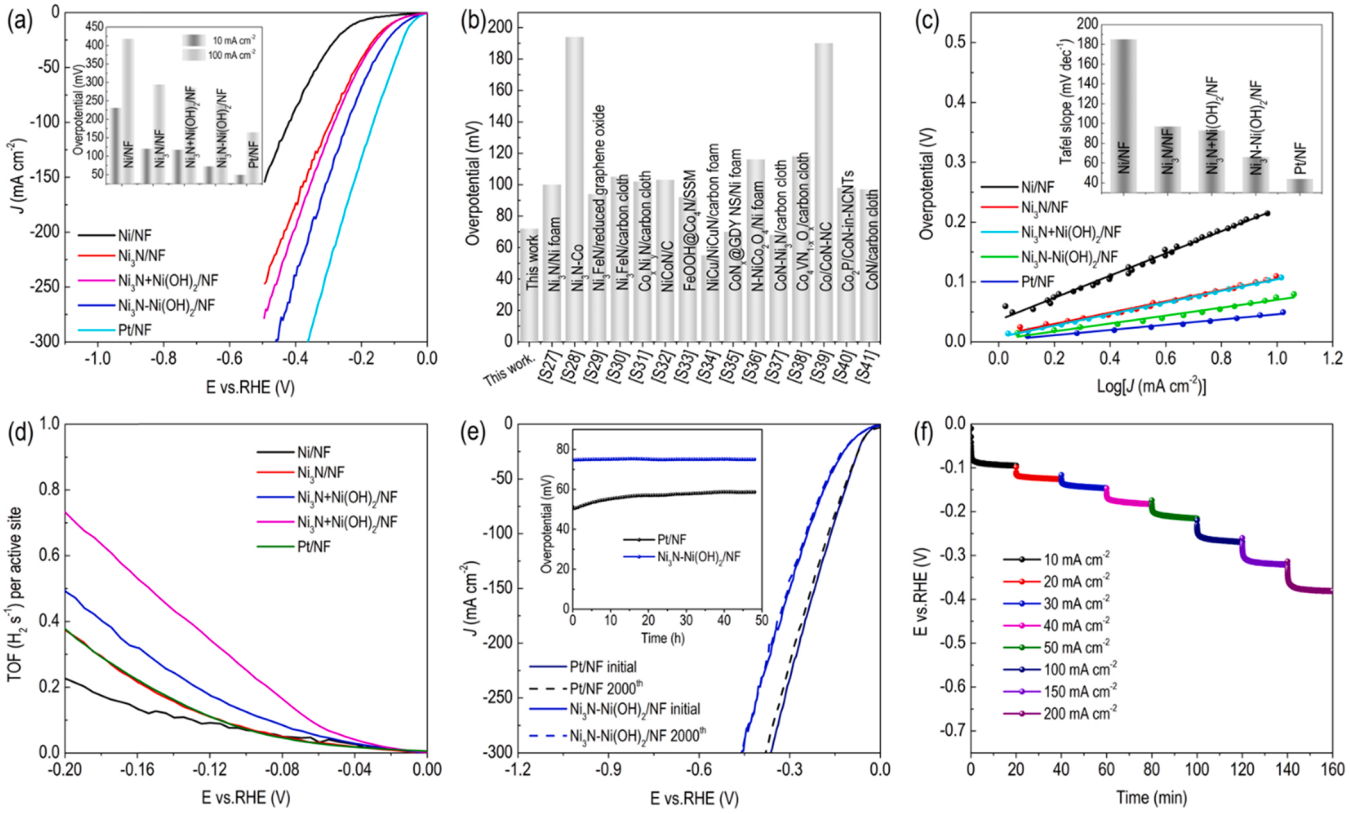

Fig. 4. (a) HER polarization curves of the fabricated catalysts in 1.0 M KOH. Inset is the plot of overpotential at the current density of − 10 and − 100 mA cm^{-2}. (b) Comparison of overpotentials of some active electrocatalysts to afford − 10 mA cm^{-2} for HER in 1.0 M KOH. (c) The corresponding Tafel plots. (d) TOF plots of those fabricated catalysts. (e) HER polarization curves of Ni_3N−$Ni(OH)_2$/NF and Pt/NF before and after CV measurements. Inset is the chronopotentiometric response of Pt/NF and Ni_3N−$Ni(OH)_2$/NF at − 10 mV cm^{-2}. (f) Multi-steps of chronopotentiometry measurement of the Ni_3N−$Ni(OH)_2$/NF electrode at various current densities.

$H_2 + 2M \leftrightarrow 2M{-}H_{ads}$ (Tafel step)

$H_2 + OH^- + M \leftrightarrow M{-}H_{ads} + H_2O + e^-$ (Heyrovsky step)

$M{-}H_{ads} + OH^- \leftrightarrow H_2O + e^- + M$ (Volmer step)

where the desorption step (Volmer step) is considered as the rate determining step for Ni due to its strong adsorption energy to H_{ads}. In this regard, the suitable HOR catalysts should possess the ability to adsorb H_{ads} species with optimal adsorption binding energy on electrocatalyst surface. Thus, the HER test can be able to employ to testify the ability of adsorption of H_{ads} species, making for the deep investigation for the mechanism of HOR [41,42].

The electrocatalytic HER performance testing was measured in 1.0 M KOH in the universal three−electrode configuration. And the commercial 20 wt% Pt/C catalyst loaded nickel foam (NF/Pt) was also measured for comparison. From their polarization curves in Fig. 4**a**, it is obviously shown that the Ni_3N−$Ni(OH)_2$/NF shows superior HER activity than other reference samples. To achieve the current density of − 10 mA cm^{-2}, the overpotential of 72 mV is required for Ni_3N−$Ni(OH)_2$/NF, which is only 23 mV larger than that of the Pt/NF, but much lower than that of Ni_3N+$Ni(OH)_2$/NF (112 mV), Ni_3N/NF (121 mV), and Ni/NF (224 mV). Such HER activity of Ni_3N−$Ni(OH)_2$/NF represents the most active HER catalyst, comparing with a majority of the reported active non−noble materials in alkaline electrolyte, as shown in Fig. 4b and Table S2. As expected, the introduction of surface hydr(oxy) oxides layer significantly decreases the reaction energy barrier and reduces the overpotential of hydrogen evolution process. From the linear fitting of their polarization curves, the corresponding Tafel curves were plotted in Fig. 4c. The Ni/NF and Ni_3N/NF show larger Tafel slope. In addition, the HER activity of those fabricated catalysts were also measured by RDE instrument. As shown in Fig. S22a, HER polarization curves of Ni, Ni_3N, Ni_3N+$Ni(OH)_2$, Ni_3N−$Ni(OH)_2$ and Pt/C indicate Ni_3N−$Ni(OH)_2$ still exhibits the improved activity compared with other Ni-based catalysts. Such results are consistent with their polarization curves in Fig. 4a with self-supported electrodes, manifesting that the surface hydr(oxy)oxides engineering can significantly boost the electrocatalytic performance. Notably, in view of above polarization curves, Fig. S22a presents that the overpotential (η) of Ni_3N−$Ni(OH)_2$ at 10 mA cm^{-2} is 91 mV, much lower than that of Ni_3N + $Ni(OH)_2$ (144 mV), Ni_3N (167 mV), Ni (229 mV), as well as Ni_3N−$Ni(OH)_2$/NF (72 mV). The decreased activity of Ni_3N−$Ni(OH)_2$ compared with Ni_3N−$Ni(OH)_2$/NF should be ascribed to the inferior powder structure which leads to the limited charge transport and mass transfer. Moreover, from their Tafel slopes in Fig. S22b, Ni_3N−$Ni(OH)_2$ has smaller slope (70 mV dec^{-1}) than Ni_3N+$Ni(OH)_2$ (96 mV dec^{-1}), Ni_3N (128 mV dec^{-1}), indicating its faster kinetics.

After coupling hydr(oxy)oxides components, the resultant Ni_3N−$Ni(OH)_2$/NF and Ni_3N+$Ni(OH)_2$/NF hold the decreased Tafel slope, especially for Ni_3N−$Ni(OH)_2$/NF, manifesting a faster kinetics of HER process, or in other word, more optimal adsorption of hydrogen on Ni_3N − $Ni(OH)_2$/NF surface. This Tafel slope of Ni_3N−$Ni(OH)_2$/NF indicates that the reaction kinetics toward HER mostly follows the Volmer−Heyrovsky mechanism, and the rate−limiting step is likely controlled by the initial water dissociation and the subsequent H*adsorption [43,44]. Therefore, the presence of surface hydr(oxy)oxides significantly promotes the water dissociation and hydrogen adsorption, thereby improving the reaction kinetics.

The electrochemical exchange current density (J_0), derived by the extrapolation of Tafel curves, can be used to further evaluate the

intrinsic specific activity toward HER. As expected, in Fig. S23, the calculated J_0 of Ni_3N−$Ni(OH)_2$/NF is 0.866 mA cm^{-2}, close to that of Pt/C benchmark (0.89 mA cm^{-2}), but larger than that of Ni/NF (0.636 mA cm^{-2}), Ni_3N/NF (0.761 mA cm^{-2}), and Ni_3N+$Ni(OH)_2$/NF (0.831 mA cm^{-2}), which indicates that the Ni_3N−$Ni(OH)_2$/NF holds the superior ability to gain-lose electrons and improved interface reaction kinetics, which is helpful for HER. In other words, the engineering of surface hydr(oxy)oxides layer evidently improves the intrinsic catalytic capability of the electrocatalysts thermodynamically.

Furthermore, the electrochemical impedance spectroscopy (EIS) was measured in potentiostatic mode from 0.01 to 10^6 Hz to investigate the kinetic behavior of electrocatalysts during HER. The corresponding Nyquist plots and the equivalent circuit model of these developed electrocatalysts for HER at given potential in 1.0 KOH are shown in Fig. S24. Obviously, the Ni_3N/NF shows the largest charge transfer resistance (R_{ct}) of 2.08 Ω. After coupling with $Ni(OH)_2$ species, the R_{ct} is decreased to be 1.20 Ω for Ni_3N+$Ni(OH)_2$/NF, while the Ni_3N−$Ni(OH)_2$/NF holds the lowest R_{ct} of 0.58 Ω, confirming that the engineering of *in-situ* formed hydr(oxy)oxide layer greatly facilitates the charge transfer rate during HER. The larger double-layer capacitance (C_{dl}) of Ni_3N−$Ni(OH)_2$/NF (Fig. S25) as comparison with other Ni-based samples manifests that the coupling interaction induced by the introduction of surface hydr(oxy)oxides layer results in more active sites. To clearly reflect the intrinsic activity of those fabricated catalysts, the cathodic LSV curves were normalized by their ECSA. As plotted in Fig. S26, Ni_3N−$Ni(OH)_2$/NF still shows the lower overpotentials compared to that of Ni_3N/NF. The surface hydr(oxy)oxides layer indicated interface coupling interaction is the primary issue for the improved HER activity. The TOF was further calculated to evaluate the intrinsic activity of those fabricated catalysts. In Fig. 4d, the TOF value of Ni_3N−$Ni(OH)_2$/NF is higher than that of Ni_3N+$Ni(OH)_2$/NF, Ni_3N/NF, and Ni/NF, which manifests that the interface coupling interaction aroused by the engineering surface hydr(oxy)oxides layer evidently improves the intrinsic activity of Ni_3N during HER process. Thus, those electrochemical measurements again demonstrate that the superior HER performance of Ni_3N−$Ni(OH)_2$/NF not only origins from sufficient active sites but also comes from the improved intrinsic activity.

Besides high electroactivity, the operation stability is another vital indicator in evaluating electrocatalysts. The continuous cyclic voltammetry (CV) and chronopotentiometry response were measured to evaluate the robustness of Ni_3N−$Ni(OH)_2$/NF and Pt/NF for H_2 evolution. As depicted in the inset of Fig. 4e, the HER overpotential of Ni_3N−$Ni(OH)_2$/NF at − 10 mA cm^{-2} only increases by 2 mV after 2000 CV cycles in 1.0 M KOH. However, the post−coated Pt/NF electrode exhibits a higher increase of 11 mV. In addition, the chronopotentiometry curves at − 10 mA cm^{-2} were collected to further discuss the durability for long−term H_2 evolution. The stable potential curve of Ni_3N−$Ni(OH)_2$/NF is observed even after 48 h in alkaline electrolyte (Fig. 4**e**), while the Pt/NF catalyst suffers from overpotential augment, especially, in the first few hours. Furthermore, multicurrent step curves of Ni_3N−$Ni(OH)_2$/NF in Fig. 4f hold almost unchanged applied potential under different current densities rising from − 10 to − 200 mA cm^{-2}, indicating its excellent durability. Post characterization, for instance, SEM image (Fig. S28a) and high-resolution XPS Ni 2p spectra (Fig. S28b), exhibits no apparent morphology and composition change of Ni_3N − $Ni(OH)_2$/NF after HER stability test, revealing the excellent mechanical stability and structure robustness. In addition, the actual H_2 yield during the HER processes was also measured to prove the practicability of this fabricated Ni_3N−$Ni(OH)_2$/NF. As plotted in Fig. S29, the experimental H_2 yield is closely reached to the theoretical value, and the Faradaic efficiency is beyond 98%, indicating that no by-products are generated during the cathodic electrochemical process.

The engineering of surface hydr(oxy)oxides layer obviously influences the HER and HOR performance of Ni_3N, further analysis about UPS was applied to investigate the electron density and electronic distribution of these fabricated Ni_3N−$Ni(OH)_2$/NF, Ni_3N/NF, and Ni/NF catalysts [45]. All the materials have electronic bands crossing the Fermi level, as shown in Fig. 5a. The signals located at 0 − 1.0 eV are directly arisen from 3d band of nickel [46]. For Ni_3N/NF and Ni_3N−$Ni(OH)_2$/NF, the broad peak located at 4 − 16 eV would be ascribed to hybridized Ni 3d and N 2p emission [47]. The maximum value of Ni 3d band has the order of Ni_3N−$Ni(OH)_2$/NF (0.663 eV) > Ni_3N/NF (0.533 eV) > Ni/NF (0.087 eV). This indicates the enlarged distance between 3d band and Fermi level from Ni/NF to Ni_3N/NF and to Ni_3N−$Ni(OH)_2$/NF. On the basis of d−band theory, the downshift of the Ni d−band center, which is close to the Fermi level, would obtain more empty antibonding state, thus weaker bond strength between catalyst surface and adsorbed H*, leading to the considerable active sites and the delicate ΔG_{H^*} on catalyst surface [28]. From the UPS results, it is concluded that the introduction of nickel hydr(oxy)oxides into nickel nitrides to engineer interfacial structure significantly renders the downshift of the Ni d−band center and the decreased adsorbate strength. According to the previous reported studies, the nickel nitrides exhibits lowest Gibbs free energy of H_{ads} intermediate than that for metal Ni, while the negatively charged Ni sites would further optimize the bond interaction between Ni sites and surface H_{ads} species. The spectroscopy measurements such as XPS and UPS verify the changed electronic structure and the downshift of Ni d band of Ni_3N−$Ni(OH)_2$/NF. Hence, the significant electronic interaction between Ni_3N and hydr(oxy)oxides layer conduces to the optimized H* adsorption energy, thereby ensuring the enhanced HER and HOR performance.

On the other hand, according to the bifunctional theory for alkaline HOR, the hydroxyl adsorption on catalyst surface also plays a critical role in the HOR activity apart from the hydrogen adsorption. Hence, the hydroxyl bonding energy (HOBE) on electrocatalyst surface was also investigated. The hydroxyl oxidative adsorption peak of those nickel−based samples were compared to discuss their HOBE [48]. As shown on the polarization curves in Ar−saturated KOH electrolyte in Fig. 5b, the Ni_3N−$Ni(OH)_2$/NF exhibits the most positive potential as compared with other two catalysts, thus obtaining the more optimal hydroxyl bonding energy. It is well accepted that the positively charged transition metal hydroxides are efficient for the adsorption of water molecule and accelerate the cleavage of O−H bonds [24]. For the synthesized Ni_3N−$Ni(OH)_2$/NF catalyst, the Ni_3N sites facilitate the H_{ads} adsorption while the hydr(oxy)oxides layer can promote the water dissociation to generate the adsorbed hydroxyl species [22,49]. In addition, the intimate interaction between Ni_3N−$Ni(OH)_2$ heterostructures making electron transfer from hydr(oxy)oxide layer to Ni_3N proved by XPS analysis, which further optimize the H adsorption energy on the heterostructure sites. The advanced electronic configuration on Ni_3N−$Ni(OH)_2$ heterostructures for Ni_3N−$Ni(OH)_2$/NF achieves the optimized hydrogen and hydroxyl adsorption energy on Ni sites, thus resulting in the outstanding HOR performance in alkaline electrolyte.

Based on the physicochemical characterizations and electrochemical measurements, the alkaline HOR pathway of Ni_3N−$Ni(OH)_2$/NF should follow the following steps in Fig. 5**c**. At the Ni_3N−$Ni(OH)_2$ heterostructures, the negatively charged Ni_3N facilitates the adsorption of hydrogen [24], and the nearby hydr(oxy)oxide species accelerate the Volmer step by prompting the hydroxyl adsorption [23], thus the synergistic effect between Ni_3N and hydr(oxy)oxides layer boosts the HOR kinetics in alkaline electrolyte. In addition, the HER mechanism occurred on Ni_3N−$Ni(OH)_2$/NF is also concluded in Fig. 5d. The surface hydr(oxy)oxide layer promotes the cleavage of O−H bonds to generate the active H intermediates [22], the adjacent Ni_3N employed as the hydrogen adsorption sites stabilize the generated H on Ni sites and the negatively transferred electrons from hydr(oxy)oxides layer to Ni_3N further optimize the bond energy of Ni−H to accelerate the formation of H_2, thus leading to the great HER activities in alkaline media. At the microscale, the boosted HOR and HER activities of Ni_3N−$Ni(OH)_2$/NF should be attributed to the enhanced water dissociation kinetics and the optimized hydrogen and hydroxyl adsorption energy on the Ni_3N−$Ni(OH)_2$ heterostructures by hydr(oxy)oxides layer introduction.

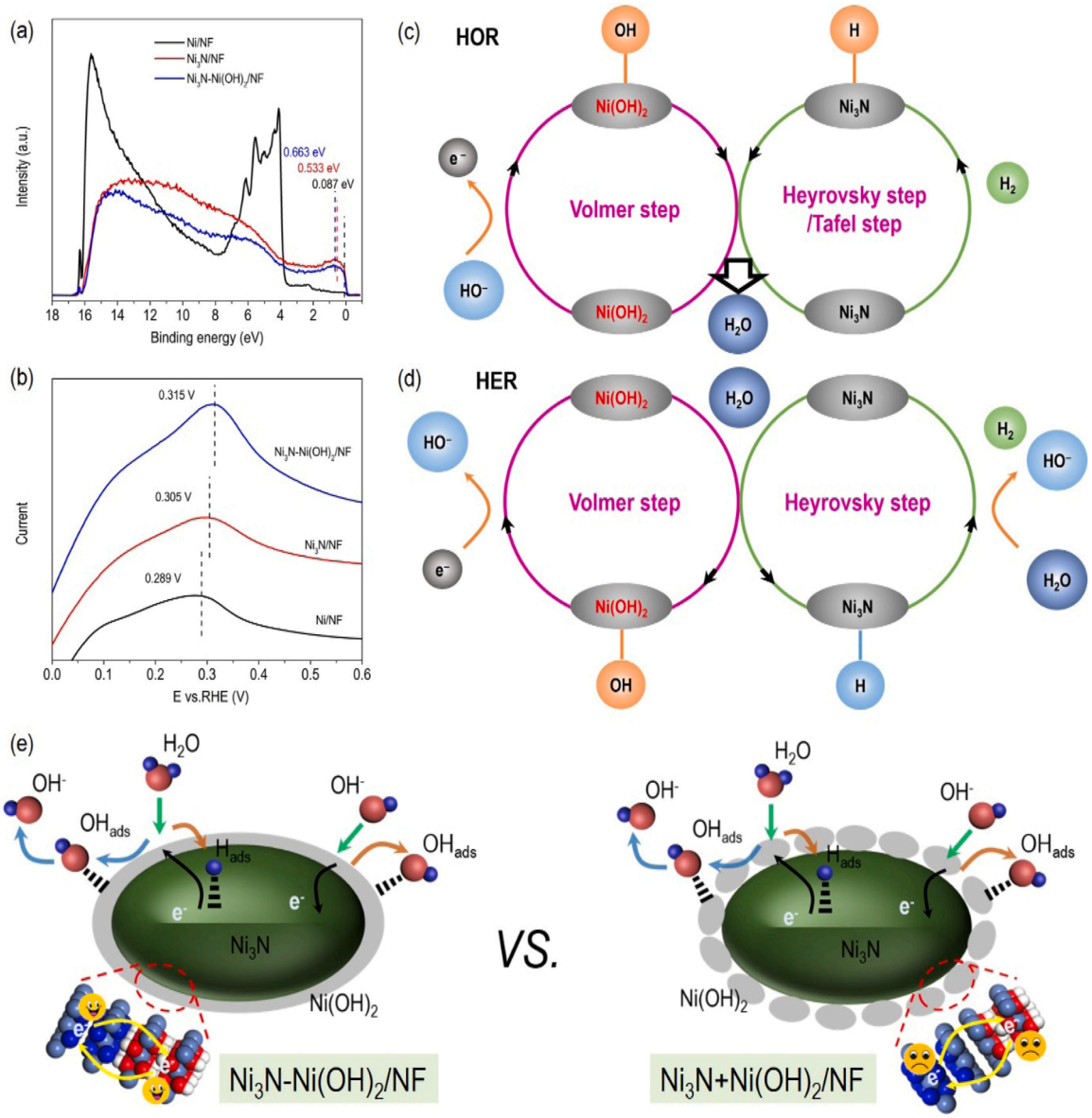

Fig. 5. (a) UPS spectra of Ni_3N−$Ni(OH)_2$/NF, Ni_3N/NF, and Ni/NF. (b) Polarization curves of Ni_3N−$Ni(OH)_2$/NF, Ni_3N/NF, and Ni/NF in Ar−saturated 1.0 M KOH electrolyte. Mechanism diagram of Ni_3N−$Ni(OH)_2$/NF for (c) HOR and (d) HER in alkaline media. (e) Schematic illustration of the synergetic Volmer steps of the alkaline HOR and HER on the developed Ni_3N−$Ni(OH)_2$/NF and Ni_3N+$Ni(OH)_2$/NF.

On the basis of the above-mentioned investigation and discussion, the enhanced hydrogen electrocatalysis performance of Ni_3N−$Ni(OH)_2$/NF as comparison with Ni_3N+$Ni(OH)_2$/NF should be ascribed to the following aspects: (a) At the nanoscale, the *in-situ* formed ultrathin hydr(oxy)oxides layer achieves the efficient synergistic effect between the hydr(oxy)oxides shell and nitrides core by reducing charge transfer resistance at heterointerfaces; moreover, the high conductivity of the Ni_3N substrate and nickel foam skeleton are also favorable for the fast electron transfer ability during the electrochemical measurements, as shown in Fig. 5e [50]. (b) The assembling of stocked nanoparticles on the 3D nickel foam network could provide the open micro-architecture, which ensures sufficient electrochemically active surface area, enhances the mass transfer ability, improves electrolyte accessibility with electrolytes, and attains gas bubbles release and mechanical durability [51]. (c) Surface nickel hydr(oxy)oxides engineering offers the desired multicomponent active species with the increased intrinsic activities, which significantly promotes water dissociation and hydroxyl adsorption during the Volmer steps toward HER and HOR, respectively, as well as optimize the adsorption energy of the hydrogen intermediates, as illustrated in Fig. 5e [52]. (d) At the atom level, the *in-situ* formed hydr(oxy)oxides layer are largely amorphous, the disordered atoms structure is favorable for providing sufficient defect sites and improving the intrinsic activities [53]. Taking the overall synergistic ability at the interfaces and multiscale structure, the developed Ni_3N−$Ni(OH)_2$ heterostructures show the remarkable HOR and HER activities as well as the robust long-term durability in alkaline electrolyte.

4. Conclusions

In this work, on the consideration of heterointerface engineering, the intimately coupled nickel nitride-nickel hydr(oxy)oxide (Ni_3N−$Ni(OH)_2$) heterostructures on nickel foam were rationally designed and fabricated. Electrochemical measurements demonstrated that this *in-situ* formed Ni_3N−$Ni(OH)_2$ heterostructures hold great apparent HOR activities, even approaching to Pt/C catalyst, while with more better tolerance to CO poisoning. Furthermore, the developed Ni_3N−$Ni(OH)_2$/

NF also exhibits impressive HER activity and stability, which are superior to most of non−precious HER electrocatalysts in alkaline media. Multiple microscopic and spectroscopic techniques reveal the significant electron transformation from surface hydr(oxy)oxide layer to Ni_3N and the downshift of the Ni d−band center. Comprehensive experiments with different referenced samples, associated with the physicochemical characterizations, demonstrate the presence of surface hydr(oxy)oxide layer facilitates the Volmer steps and the negatively charged Ni_3N sites optimize the adsorption of reaction intermediates, hence resulting in the boosted hydrogen electrocatalysis in alkaline media. Our work reported herein not only provides one of low cost and efficient alkaline HOR catalysts for HEMFCs, but also highlights the significant potential of surface emerging of nickel nitrides to improve the electrocatalytic performance.

CRediT authorship contribution statement

Jin-Tao Ren: Conceptualization, Methodology, Investigation, Writing − original draft. **Yan-Su Wang**: Physicochemical characterization. **Yue-Jun Song**: Physicochemical characterization. **Lei Chen**: Physicochemical characterization. **Zhong-Yong Yuan**: Supervision, Project administration.

Declaration of Competing Interest

The authors declare that they have no known competing financial interests or personal relationships that could have appeared to influence the work reported in this paper.

Acknowledgements

This work was supported by the National Natural Science Foundation of China (21875118, 22179065, and 22105108), the Natural Science Foundation of Tianjin (19JCZDJC37700), and China Postdoctoral Science Foundation (2020M680860).

Appendix A. Supporting information

Supplementary data associated with this article can be found in the online version at doi:10.1016/j.apcatb.2022.121279.

References

[1] D.G. Nocera, Solar fuels and solar chemicals industry, Acc. Chem. Res. 50 (2017) 616–619.
[2] B. You, Y. Sun, Innovative strategies for electrocatalytic water splitting, Acc. Chem. Res. 51 (2018) 1571–1580.
[3] H.A. Gasteiger, S.S. Kocha, B. Sompalli, F.T. Wagner, Activity benchmarks and requirements for Pt, Pt-alloy, and non-Pt oxygen reduction catalysts for PEMFCs, Appl. Catal. B 56 (2005) 9–35.
[4] I. Ledezma-Yanez, W.D.Z. Wallace, P. Sebastián-Pascual, V. Climent, J.M. Feliu, M. T. Koper, Interfacial water reorganization as a pH-dependent descriptor of the hydrogen evolution rate on platinum electrodes, Nat. Energy 2 (2017) 17031.
[5] S. Deng, X. Liu, X. Guo, T. Zhao, Y. Lu, J. Cheng, K. Chen, T. Shen, Y. Zhu, D. Wang, Insight into the hydrogen oxidation electrocatalytic performance enhancement on Ni via oxophilic regulation of MoO_2, J. Energy Chem. 54 (2020) 202–207.
[6] F. Song, W. Li, J. Yang, G. Han, P. Liao, Y. Sun, Interfacing nickel nitride and nickel boosts both electrocatalytic hydrogen evolution and oxidation reactions, Nat. Commun. 9 (2018) 4531.
[7] W. Sheng, Z. Zhuang, M. Gao, J. Zheng, J.G. Chen, Y. Yan, Correlating hydrogen oxidation and evolution activity on platinum at different pH with measured hydrogen binding energy, Nat. Commun. 6 (2015) 5848.
[8] Y. Cong, B. Yi, Y. Song, Hydrogen oxidation reaction in alkaline media: From mechanism to recent electrocatalysts, Nano Energy 44 (2018) 288–303.
[9] Y. Zheng, Y. Jiao, A. Vasileff, S.-Z. Qiao, The hydrogen evolution reaction in alkaline solution: from theory, single crystal models, to practical electrocatalysts, Angew. Chem. Int. Ed. 57 (2018) 7568–7579.
[10] J.-T. Ren, Z.-Y. Yuan, Heterojunction-induced nickel-based oxygen vacancies on N-enriched porous carbons for enhanced alkaline hydrogen oxidation and oxygen reduction, Mater. Chem. Front. 5 (2021) 2399–2408.
[11] J. Lai, B. Huang, Y. Chao, X. Chen, S. Guo, Strongly coupled nickel-cobalt nitrides/carbon hybrid nanocages with pt-like activity for hydrogen evolution catalysis, Adv. Mater. 31 (2019) 1805541.
[12] B.P. Setzler, Z. Zhuang, J.A. Wittkopf, Y. Yan, Activity targets for nanostructured platinum group-metal-free catalysts in hydroxide exchange membrane fuel cells, Nat. Nanotechnol. 11 (2016) 1020–1025.
[13] H. Mistry, A.S. Varela, S. Kuehl, P. Strasser, B.R. Cuenya, Nanostructured electrocatalysts with tunable activity and selectivity, Nat. Rev. Mater. 1 (2016) 16009.
[14] Z.W. Seh, J. Kibsgaard, C.F. Dickens, I.B. Chorkendorff, J.K. Norskov, T. F. Jaramillo, Combining theory and experiment in electrocatalysis: insights into materials design, Science 355 (2017) eaad4998.
[15] W. Ni, T. Wang, P.A. Schouwink, Y.C. Chuang, H.M. Chen, X. Hu, Efficient hydrogen oxidation catalyzed by strain-engineered nickel nanoparticles, Angew. Chem. Int. Ed. 59 (2020) 10797–10801.
[16] M. Wang, H. Yang, J. Shi, Y. Chen, Y. Zhou, L. Wang, S. Di, X. Zhao, J. Zhong, T. Cheng, W. Zhou, Y. Li, Alloying nickel with molybdenum significantly accelerates alkaline hydrogen electrocatalysis, Angew. Chem. Int. Ed. 60 (2021) 5771–5777.
[17] G. Chen, C. Xu, X. Huang, J. Ye, L. Gu, G. Li, Z. Tang, B. Wu, H. Yang, Z. Zhao, Z. Zhou, G. Fu, N. Zheng, Interfacial electronic effects control the reaction selectivity of platinum catalysts, Nat. Mater. 15 (2016) 564–569.
[18] B. You, X. Liu, G. Hu, S. Gul, J. Yano, D.-E. Jiang, Y. Sun, Universal surface engineering of transition metals for superior electrocatalytic hydrogen evolution in neutral water, J. Am. Chem. Soc. 139 (2017) 12283–12290.
[19] Y. Yang, X. Sun, G. Han, X. Liu, X. Zhang, Y. Sun, M. Zhang, Z. Cao, Y. Sun, Enhanced electrocatalytic hydrogen oxidation on Ni/NiO/C derived from a nickel-based metal-organic framework, Angew. Chem. Int. Ed. 131 (2019) 10754–10759.
[20] F. Yang, X. Bao, P. Li, X. Wang, G. Cheng, S. Chen, W. Luo, Boosting hydrogen oxidation activity of Ni in alkaline media through oxygen-vacancy-rich CeO_2/Ni heterostructures, Angew. Chem. Int. Ed. 58 (2019) 14179–14183.
[21] T. Wang, M. Wang, H. Yang, M. Xu, C. Zuo, K. Feng, M. Xie, J. Deng, J. Zhong, W. Zhou, T. Cheng, Y. Li, Weakening hydrogen adsorption on nickel via interstitial nitrogen doping promotes bifunctional hydrogen electrocatalysis in alkaline solution, Energy Environ. Sci. 12 (2019) 3522–3529.
[22] Z. Dong, F. Lin, Y. Yao, L. Jiao, Crystalline $Ni(OH)_2$/amorphous $NiMoO_x$ mixed-catalyst with Pt-Like performance for hydrogen production, Adv. Energy Mater. 9 (2019) 1902703.
[23] Y. Wang, L. Chen, X. Yu, Y. Wang, G. Zheng, Superb alkaline hydrogen evolution and simultaneous electricity generation by Pt-decorated Ni_3N nanosheets, Adv. Energy Mater. 7 (2017) 1601390.
[24] B. You, Y. Zhang, Y. Jiao, K. Davey, S.Z. Qiao, Negative charging of transition-metal phosphides via strong electronic coupling for destabilization of alkaline water, Angew. Chem. Int. Ed. 58 (2019) 11796–11800.
[25] L. Gao, X. Cui, C.D. Sewell, J. Li, Z. Lin, Recent advances in activating surface reconstruction for the high-efficiency oxygen evolution reaction, Chem. Soc. Rev. 50 (2021) 8428–8469.
[26] A. Sivanantham, P. Ganesan, A. Vinu, S. Shanmugam, Surface activation and reconstruction of non-oxide-based catalysts through in situ electrochemical tuning for oxygen evolution reactions in alkaline media, ACS Catal. 10 (2020) 463–493.
[27] C. Ray, S.C. Lee, B. Jin, A. Kundu, J.H. Park, S.C. Jun, Conceptual design of three-dimensional CoN/Ni_3N-coupled nanograsses integrated on N-doped carbon to serve as efficient and robust water splitting electrocatalysts, J. Mater. Chem. A 6 (2018) 4466–4476.
[28] D. Gao, J. Zhang, T. Wang, W. Xiao, K. Tao, D. Xue, J. Ding, Metallic Ni_3N nanosheets with exposed active surface sites for efficient hydrogen evolution, J. Mater. Chem. A 4 (2016) 17363–17369.
[29] T. Liu, M. Li, C. Jiao, M. Hassan, X. Bo, M. Zhou, H.-L. Wang, Design and synthesis of integrally structured Ni_3N nanosheets/carbon microfibers/Ni_3N nanosheets for efficient full water splitting catalysis, J. Mater. Chem. A 5 (2017) 9377–9390.
[30] X. Feng, H. Wang, X. Bo, L. Guo, Bimetal-organic framework-derived porous rodlike cobalt/nickel nitride for All-pH value electrochemical hydrogen evolution, ACS Appl. Mater. Interfaces 11 (2019) 8018–8024.
[31] B. Cao, G.M. Veith, J.C. Neuefeind, R.R. Adzic, P.G. Khalifah, Mixed close-packed cobalt molybdenum nitrides as non-noble metal electrocatalysts for the hydrogen evolution reaction, J. Am. Chem. Soc. 135 (2013) 19186–19192.
[32] A. Wu, Y. Xie, H. Ma, C. Tian, Y. Gu, H. Yan, X. Zhang, G. Yang, H. Fu, Integrating the active OER and HER components as the heterostructures for the efficient overall water splitting, Nano Energy 44 (2018) 353–363.
[33] M. Wu, Q. Wei, G. Zhang, J. Qiao, M. Wu, J. Zhang, Q. Gong, S. Sun, Fe/Co Double Hydroxide/Oxide Nanoparticles on N-Doped CNTs as highly efficient electrocatalyst for rechargeable liquid and Quasi-Solid-State zinc-air batteries, Adv. Energy Mater. 8 (2018) 1801836.
[34] R. Subbaraman, D. Tripkovic, K.-C. Chang, D. Strmcnik, A.P. Paulikas, P. Hirunsit, M. Chan, J. Greeley, V. Stamenkovic, N.M. Markovic, Trends in activity for the water electrolyser reactions on 3d M(Ni,Co,Fe,Mn) hydr(oxy)oxide catalysts, Nat. Mater. 11 (2012) 550–557.
[35] Z. Zeng, K.-C. Chang, J. Kubal, N.M. Markovic, J. Greeley, Stabilization of ultrathin (hydroxy) oxide films on transition metal substrates for electrochemical energy conversion, Nat. Energy 2 (2017) 17070.
[36] S. Kabir, K. Lemire, K. Artyushkova, A. Roy, M. Odgaard, D. Schlueter, A. Oshchepkov, A. Bonnefont, E. Savinova, D.C. Sabarirajan, P. Mandal, E. J. Crumlin, I.V. Zenyuk, P. Atanassov, A. Serov, Platinum group metal-free NiMo hydrogen oxidation catalysts: high performance and durability in alkaline exchange membrane fuel cells, J. Mater. Chem. A 5 (2017) 24433–24443.
[37] S. Deng, X. Liu, T. Huang, T. Zhao, Y. Lu, J. Cheng, T. Shen, J. Liang, D. Wang, MoO_2 modulated electrocatalytic properties of Ni: investigate from hydrogen oxidation reaction to hydrogen evolution reaction, Electrochim. Acta 324 (2019), 134892.

[38] W. Ni, A. Krammer, C.S. Hsu, H.M. Chen, A. Schuler, X. Hu, Ni_3N as an active hydrogen oxidation reaction catalyst in alkaline medium, Angew. Chem. Int. Ed. 58 (2019) 7445–7449.
[39] Z. Zhuang, S.A. Giles, J. Zheng, G.R. Jenness, S. Caratzoulas, D.G. Vlachos, Y. Yan, Nickel supported on nitrogen-doped carbon nanotubes as hydrogen oxidation reaction catalyst in alkaline electrolyte, Nat. Commun. 7 (2016) 10141.
[40] L. Gao, Y. Wang, H. Li, Q. Li, N. Ta, L. Zhuang, Q. Fu, X. Bao, A nickel nanocatalyst within a h-BN shell for enhanced hydrogen oxidation reactions, Chem. Sci. 8 (2017) 5728–5734.
[41] I. Bakos, A. Paszternák, D. Zitoun, Pd/Ni synergestic activity for hydrogen oxidation reaction in alkaline conditions, Electrochim. Acta 176 (2015) 1074–1082.
[42] J. Durst, A. Siebel, C. Simon, F. Hasche, J. Herranz, H.A. Gasteiger, New insights into the electrochemical hydrogen oxidation and evolution reaction mechanism, Energy Environ. Sci. 7 (2014) 2255–2260.
[43] J. Zhang, T. Wang, P. Liu, Z. Liao, S. Liu, X. Zhuang, M. Chen, E. Zschech, X. Feng, Efficient hydrogen production on $MoNi_4$ electrocatalysts with fast water dissociation kinetics, Nat. Commun. 8 (2017) 15437.
[44] J. Mao, C.-T. He, J. Pei, W. Chen, D. He, Y. He, Z. Zhuang, C. Chen, Q. Peng, D. Wang, Y. Li, Accelerating water dissociation kinetics by isolating cobalt atoms into ruthenium lattice, Nat. Commun. 9 (2018) 4958.
[45] T. Kambe, R. Sakamoto, K. Hoshiko, K. Takada, M. Miyachi, J.-H. Ryu, S. Sasaki, J. Kim, K. Nakazato, M. Takata, π-Conjugated nickel bis (dithiolene) complex nanosheet, J. Am. Chem. Soc. 135 (2013) 2462–2465.
[46] J.-H. Dou, L. Sun, Y. Ge, W. Li, C.H. Hendon, J. Li, S. Gul, J. Yano, E.A. Stach, M. Dincă, Signature of metallic behavior in the metal–organic frameworks M3 (hexaiminobenzene)2 (M= Ni, Cu), J. Am. Chem. Soc (2017) 13608–13611.
[47] K. Xu, P. Chen, X. Li, Y. Tong, H. Ding, X. Wu, W. Chu, Z. Peng, C. Wu, Y. Xie, Metallic nickel nitride nanosheets realizing enhanced electrochemical water oxidation, J. Am. Chem. Soc. 137 (2015) 4119–4125.
[48] J. Ohyama, T. Sato, Y. Yamamoto, S. Arai, A. Satsuma, Size specifically high activity of Ru nanoparticles for hydrogen oxidation reaction in alkaline electrolyte, J. Am. Chem. Soc. 135 (2013) 8016–8021.
[49] R. Majee, A. Kumar, T. Das, S. Chakraborty, S. Bhattacharyya, Tweaking nickel with minimal silver in a heterogeneous alloy of decahedral geometry to deliver platinum-like hydrogen evolution activity, Angew. Chem. Int. Ed. 59 (2020) 2881–2889.
[50] Q. Qian, J. Zhang, J. Li, Y. Li, X. Jin, Y. Zhu, Y. Liu, Z. Li, A. El-Harairy, C. Xiao, G. Zhang, Y. Xie, Artificial heterointerfaces achieve delicate reaction kinetics towards hydrogen evolution and hydrazine oxidation catalysis, Angew. Chem. Int. Ed. 60 (2021) 5984–5993.
[51] J. Wang, N. Zang, C. Xuan, B. Jia, W. Jin, T. Ma, Self-supporting electrodes for gas-involved key energy reactions, Adv. Funct. Mater. 31 (2021) 2104620.
[52] B. You, S.Z. Qiao, Destabilizing alkaline water with 3d-Metal (Oxy)(Hydr)oxides for improved hydrogen, Evol., Chem. Eur. J. 27 (2021) 553–564.
[53] X. Gao, X. Li, Y. Yu, Z. Kou, P. Wang, X. Liu, J. Zhang, J. He, S. Mu, J. Wang, Synergizing aliovalent doping and interface in heterostructured NiV Nitride@ Oxyhydroxide core-shell nanosheet arrays enables efficient oxygen evolution, Nano Energy 85 (2021), 105961.